Journal of Colloid and Interface Science 538 (2019) 387–396

Contents lists available at ScienceDirect

Journal of Colloid and Interface Science

journal homepage: www.elsevier.com/locate/jcis

Regular Article

Interfacial uploading of luminescent hexamolybdenum cluster units onto amino-decorated silica nanoparticles as new design of nanomaterial for cellular imaging and photodynamic therapy

Julia Elistratova [a,*], Alsu Mukhametshina [a], Kirill Kholin [a], Irek Nizameev [a], Maksim Mikhailov [b], Maxim Sokolov [b], Rafil Khairullin [a,c], Regina Miftakhova [c], Ghazal Shammas [c], Marsil Kadirov [a], Konstantin Petrov [a], Albert Rizvanov [c], Asiya Mustafina [a]

[a] Arbuzov Institute of Organic and Physical Chemistry, FRC Kazan Scientific Center of RAS, Arbuzov str., 8, 420088 Kazan, Russia
[b] Nikolaev Institute of Inorganic Chemistry, 3 Acad. Lavrentiev Prosp., Novosibirsk, Russia
[c] Institute of Fundamental Medicine and Biology, Kazan Federal University, Kremlyovskaya str., 18, 420008 Kazan, Russia

GRAPHICAL ABSTRACT

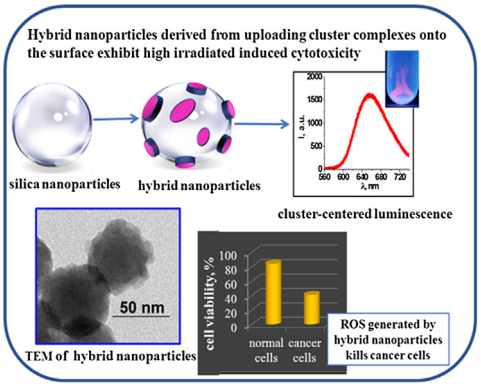

ARTICLE INFO

Article history:
Received 17 October 2018
Revised 30 November 2018
Accepted 3 December 2018
Available online 4 December 2018

Keywords:
Photodynamic therapy
Silica nanoparticles
Hexamolybdenum cluster
Cell internalization
Luminescence
Adsorption

ABSTRACT

The present work introduces a facile synthetic route to embed phosphorescent $K_2[\{Mo_6I_8\}I_6]$ and $(nBu_4N)_2[\{Mo_6I_8\}(CH_3COO)_6]$ clusters (C) onto silica-water interface of amino-decorated silica nanoparticles (SNs, 60 ± 6 nm). The assembled C-SNs gain in the luminescence intensity, which remains stable within three months after their assembly. High uptake capacity of the clusters (8700 of $K_2[\{Mo_6I_8\}I_6]$ and 6500 of $(nBu_4N)_2[\{Mo_6I_8\}(CH_3COO)_6]$ per the each nanoparticle) derives from ionic self-assembly and coordination bonds between the cluster complexes and ionic (amino- and siloxy-) groups at the silica surface. The coordination *via* amino- or siloxy-groups restricts aquation and hydrolysis of the embedded clusters, in comparison with the parent $K_2[\{Mo_6I_8\}I_6]$ and $(nBu_4N)_2[\{Mo_6I_8\}(CH_3COO)_6$. High potential of the assembled nanoparticles in the ROS generation was revealed by EPR measurements facilitated by spin trapping. The high positive charge and convenient colloid stability of the assembled C-SNs hybrids are the prerequisite for their efficient cellular uptake, which is exemplified in the work by MCF-7 cell line. The measured dark and photoinduced cytotoxicity of the C-SNs hybrids reveals significant photodynamic therapy effect on the MCF-7 cancer cell line versus the normal cells. This effect is entirely due to the embedded clusters and is dependent on the chemical composition of the cluster.

* Corresponding author.
E-mail address: 969_969@bk.ru (J. Elistratova).

https://doi.org/10.1016/j.jcis.2018.12.013
0021-9797/

1. Introduction

Multifunctional nanomaterials have gained much attention in the last decade, not in the least due to their biomedical applicability. In this respect, luminescence and therapeutic effect are very important properties of the multifunctional nanomaterials, in particular for imaging and therapy of cancer [1–3]. This fits nicely into the theranostics paradigm, which involves using nanoscience to unite diagnostic (in our case, luminescent) and therapeutic (photodynamic therapy) applications in a single agent, allowing for diagnosis, drug delivery and treatment response monitoring. A major challenge for nanotechnology at this point is to elaborate non-toxic and aging-resistant phosphorescent nanomaterials emitting above 650 nm in order to fit into the so-called biological transparency window where the interfering effect of light absorption or fluorescence of biological background is insignificant. Hexanuclear (hexamolybdenum and hexarhenium) cluster complexes emitting at 650–750 nm range recently have found their way on the top of research activity in the area [4–8]. This interest is in particular sustained by their ability to generate singlet oxygen under light irradiation, which, in turn, is a promising basis for photodynamic therapy applications [9]. Their robust and easily assembled structure features a rigid cluster core $\{M_6X_8\}$ (M = Mo, W, Re; X is halide or chalcogenide) with firmly attached, but exchangeable six terminal ligands, *L*, giving overall $[\{M_6X_8\}L_6]$ composition for stable cluster entity, which can be cationic, neutral, or, what is most common, anionic, depending on the specific nature of M, X, and L. Unfortunately, negative charge of the cluster complexes restricts their cellular uptake. The $\{Mo_6I_8L_6\}$ clusters are particularly attractive, given their easy preparation, relative low cost and superior emissive properties. A major handicap here is their tendency to hydrolyze already in neutral aqueous solutions, which cancels their emission [8]. Moreover, formation of sparingly soluble aqua-hydroxo complexes $[Mo_6I_8(OH)_4(H_2O)_2]$ leads to microsized aggregates with acute toxicity for living organisms [8].

Fluorophores emitting in red and far-red regions embedded in silica nanoparticles are highlighted as the best basis for developing of multifunctional nanomaterials for biomedical purposes [10–12]. Easy silica surface functionalization enables to tune a cellular uptake behavior by means of convenient surface decoration with specific functional groups or biomolecules [13–16]. Convenient size of silica nanoparticles is also highlighted as a factor facilitating their cell internalization through endocytosis [17–20]. Thus, molecular or ionic compounds exhibiting required functional properties but poor cell internalization should be embedded to silica nanoparticles in order to activate their cellular uptake. In this connection, a series of publications report embedding of the hexamolybdenum cluster complexes into silica nanoparticles [21–24]. These reports indicate the possibility of fabrication of silica nanoparticles with red cluster-centered long-lived luminescence. Nevertheless, both partial hydrolysis of the cluster complexes in the process of the cluster-nanoparticle composites preparation and inaccessibility of a sizeable fraction of the embedded clusters to oxygen represent major shortcomings of this approach [21].

Literature sources indicate the ionic assembling method based on efficient electrostatic attraction of the cluster anions to positively charged counter-ions as powerful tool to embed the cluster complexes into hard [25,26] or soft nanoparticles [4]. Such non-covalent approach results in safe embedding of the cluster complexes into the nanomaterial without any degradation, which is the reason for the cluster-centered luminescence remaining unchanged in the nanomaterial. Moreover, wrapping of the cluster anions by polyelectrolyte or triblock copolymer molecules also results in high stability of the cluster-centered luminescence, while the degradation of the cluster complexes in neutral diluted aqueous solutions is significant within one day [4,27]. The present report introduces interfacial adsorption of $[\{Mo_6I_8\}I_6]^{2-}$ and $[\{Mo_6I_8\}(CH_3COO)_6]^{2-}$ cluster anions onto amino-modified surface of silica nanoparticles (SNs) as facile approach of their efficient loading by the cluster anions. The results indicate the impact of amino- and siloxy-groups at the SNs surface on the adsorption of the cluster anions through both ionic self-assembly and coordination bonds formation. Thus, amino-decorated SNs are introduced herein as prime reason for hybrid cluster nanoparticles $[\{Mo_6I_8\}(CH_3COO)_6]$-SNs and $[\{Mo_6I_8\}I_6$-SNs. The well-known enhanced uptake capacity of amino-decorated compared vs. "naked" silica nanoparticles confirms the validity of such approach. Furthermore, we introduce assembly of the embedded nanoparticles with triblock copolymer molecules as a means of enhancing their colloid stability. High positive charge, stable in time luminescence of the assembled nanoparticles are highlighted as a prerequisite for their applicability as cellular contrast agents. The present work also demonstrates that the luminescence of the assembled nanoparticles enables to quantitatively evaluate the cellular uptake behavior of C-SNs.

Taking into account that ROS (reactive oxygen species) generation takes place at nanoparticle/water interface, any surface coating will dramatically affect ROS generation [21,28,29]. High potential of the assembled C-SNs in ROS generation is revealed by EPR measurements with the use of the well-known spin trap DMPO [30–32]. The C-SNs hybrids show low cytotoxic effect without irradiation, but significant cytotoxicity under the irradiation which is also represented for the cancer cell line MCF-7, thus fulfilling another prerequisite for their applicability in theranostics. Specific incubation time (6 h) is required for significant photodynamic therapy effect on the cancer versus normal cells exemplified by HSF cell line. This reflects different cell internalization of the assembled C-SNs into the cancer and normal cells.

2. Experimental section

2.1. Materials

Tetraethyl orthosilicate (TEOS, 98%), ammonium hydroxide (28–30%), *n*-heptanol (98%), 3-aminopropyltriethoxysilane (APTES, 99%), 4-morpholineethanesulfonic acid hydrate (MES, 99%), β-alanine and fluorescamine were purchased from Acros Organics and used without further purification. Triton X-100, cyclohexane (99%) and triblock copolymer $(PEO)_{13}(PPO)_{30}(PEO)_{13}$ (L64), 5,5-dimethyl-pyrroline N-oxide (DMPO) were purchased from Sigma-Aldrich.

$[K(diglyme)(CH_3CN)]_2[Mo_6I_{14}]$ and $(nBu_4N)_2[\{Mo_6I_8\}(CH_3COO)_6]^{2-}$ were synthesized in accordance with the previously published procedures [27,33].

TEOS was purified by distillation.

Synthesis of amino-modified silica nanoparticles (SNs) was performed through the water-in-oil microemulsion procedure. The synthetic mixture from Triton X-100 (8.63 g), cyclohexane (33.75 mL), *n*-heptanol (8.1 mL) and 2.16 mL of water was stirred for 15 min, followed by the addition of 0.27 mL of aqueous ammonia (28–30%). After stirring for 15 min, TEOS (0.23 mL) was added to the mixture, followed by further stirring for 24 h. Then, TEOS (0.23 mL) was added again, and the mixture was stirred for 30 min. After addition of APTES (0.045 mL), the mixture was stirred for another 24 h. The synthesized nanoparticles were separated from the microemulsion by adding acetone, centrifuging, and washing with acetone/ethanol mixture (1:1), ethanol (once) and water (several times).

Fluorescamine-based procedure was applied for quantitative essay of amino groups on the surface of the aminomodified SNs [34].

The ionic assembly of the SNs with $[\{Mo_6I_8\}I_6]^{2-}$ and $[\{Mo_6I_8\}(CH_3COO)_6]^{2-}$ cluster anions has been performed according to the following procedure. An L64-based solution (0.3 mM) of the cluster complexes (0.035 mM) was mixed with the aqueous colloids of the SNs (0.5 $g{\cdot}L^{-1}$). The mixture was stirred by means of Shaker Hei-MIX Multi Reax for 10 min and sonicated for 15 min with further phase separation by centrifugation at 25 °C (15000 rpm) in order to get rid of excess cluster units and L64. Afterwards, the assembled nanoparticles were washed by water and dispersed in water or buffer solutions.

MES buffer (50 mM, pH 7.0) was applied for the sample preparation.

2.2. Methods

Transmission electron microscopy images of silica nanoparticles were obtained using a Hitachi HT7700 apparatus (Japan). The images were acquired under an accelerating voltage of 100 kV. Samples were ultrasonicated in absolute ethanol for 10 min and then dispersed on 200 mesh copper grids with continuous formvar support films.

The steady-state emission spectra were recorded on a fluorescence spectrophotometer Hitachi F-7100. Excitation of samples was performed at 380 nm.

The separation of the colloids was performed by centrifuge MPW-351/R with the temperature control within 20-40 °C.

Mo and Si in the colloids were measured using inductively coupled plasma optical emission spectrometry (ICP-OES) on an iCAP 6300 DUO analyzer by Varian Thermo Scientific Company equipped with a CID detector. This spectrometer enables simultaneous measurement of peak heights within 166–867 nm range. The optical resolution is <0.007 nm at 200 nm. The working frequency is 27.12 MHz. Together, the radial and axial view configurations enable optimal peak height measurements with suppressed spectral noises. The experimentally observed Mo (spectral line – 202.030 nm) and Si (spectral line – 251.611 nm) concentrations are summarized in Table S3.

The dynamic light scattering (DLS) measurements and zeta potential values of nanoparticles in aqueous dispersions were carried out using Zetasizer Nano ZS (Malvern Instruments). All samples were prepared in twice distilled water filtered through 0.45 μm Millipore nylon membrane filter. All samples with nanoparticles were ultrasonicated for 30 min before measurements.

The ESR experiments were carried out on an ELEXSYS E500 ESR X-band spectrometer. The ESR spectra were simulated with WinSim free software (version 0.96, National Institute of Environmental Health Sciences). The irradiation of the samples was done by light emitting diode (420 nm) or UV-lamp Vilber Lourmat (365 nm) at a distance of 35 cm from the light source.

pHs of solutions were controlled with Microprocessor pH meter Hanna Instruments HI 212 (Germany). The pH-meter was calibrated with standard aqueous buffer solutions.

2.2.1. Cultivation of the cell lines

MCF-7 (human breast cancer cell line) was obtained from American Type Culture Collection (ATCC, Manassas, VA). The cell line was maintained and propagated in RPMI-1640 culture medium supplemented with 10% fetal bovine serum, 50 units/mL penicillin, 50 mg/mL streptomycin, and 2 mM L-glutamine. MCF-7 cells were maintained at 37 °C in a humidified atmosphere of 5% CO_2 as a monolayer culture. HSF (human skin fibroblast) were isolated by "skin explant culture" techniques [35]. HSF cells were maintained at 37 °C in a humidified atmosphere of 5% CO_2 as a monolayer culture.

2.2.2. Cytotoxicity of nanoparticles

The cytotoxicity induced by nanoparticles was investigated by 3-(4,5-dimethylthiazol-2-yl)-2,5-diphenyltetrazolium bromide (MTT) assay. MCF-7 cells were grown in RPMI-1640 at 37 °C under 5% CO_2 in a humidified incubator. Cells were trypsinized, harvested, counted and seeded in 96-well plates at a density of $5{\cdot}10^3$ cells in 200 μL medium per well. The medium was then replaced with the complete cell culture medium RPMI-1640 containing nanoparticles in the concentration range 1.5–121.5 ng/mL with further incubation for 6 h. After double washing with PBS the cells were incubated with cell culture medium containing 500 μg/mL MTT solution and were added to the wells. After 3 h of the incubation the medium was removed by aspiration, and formazan crystals were solubilized with DMSO. The plates were then shaken for 10 s, and optical density at 565 nm was determined with a microplate reader (Tecan Infinite 200 Pro, TECAN, Switzerland). The relative cell viability in relation to control was calculated by [A]np/[A]control × 100, where [A]np is the absorbance of the wells with nanoparticles and [A]control is the absorbance of control wells containing cell culture medium without nanoparticles. Three independent experiments and three replicates were performed for each experiment.

2.2.3. Quantitative analysis of nanoparticle uptake

For nanoparticle uptake analysis, MCF-7 cells were seeded into 96-well plates at a density of $5{\cdot}10^3$ cells in 200 μL of RPMI medium. The cells were incubated with the nanoparticles (concentration range 1.5–121.5 ng/mL) for 6 h. The cells were washed twice with 200 μL of PBS, and fresh cell culture media were added. The fluorescence intensity of the nanoparticles in each well was then measured with a microplate reader (Tecan Infinite 200 Pro, TECAN, Switzerland) with excitation at 380 nm. The fluorescence intensity was detected at 750 nm. Cells incubated without nanoparticles were used for negative control. The fluorescence of the unwashed wells with the nanoparticles (121.5, 40.5, 13.5, 4.5 and 1.5 ng/mL) measured in triplicates was used for plotting of the calibration curves for determination of the amount of nanoparticles internalized in the cells.

2.2.4. Photodynamic treatment

MCF-7 cells were seeded 96-well plates at a density of $3{\cdot}10^3$ cells in 200 μL RPMI medium per well and incubated for 24 h prior to the addition of the nanoparticles. The media were then replaced with complete cell culture medium RPMI-1640 containing the nanoparticles (121.5 ng/mL). After 6 h the cells were washed twice with PBS and supplemented with a fresh medium and irradiated by light emitting diode (LED) at 420 nm for 15 min at a distance of 30 mm to the LED with a light dose of 24 J/cm^2. Next, the cells were washed with fresh medium, and plates were returned to the incubator for 24 h. The viability of the irradiated cells was determined by the MTT assay (described above) within 24 h after the irradiation. The relative cell viability compared to control wells containing the cell culture medium incubated with nanoparticles but non-treated by the irradiation was calculated by [A]irr/[A]control × 100. Here [A]irr is the absorbance of the irradiated wells and [A]control is the absorbance of the control wells without irradiation. The relative cell viability was calculated by [A]x/[A]control × 100, where Acontrol is the absorbance of the control cells (MCF-7 or HSF cells without the SNs) non-treated by the irradiation. [A]x is the absorbance of the cells incubated by the SNs which are either treated or non-treated by the irradiation. Three independent experiments and three replicates for each experiment were performed. The statistical analysis of the data was done by Mann-Whitney tests with the statistical significance at $p < 0.05$.

3. Results and discussion

3.1. Preparation of the nanobeads and their assembly with the clusters

As it has been mentioned above, convenient decoration of silica nanoparticles is the main prerequisite for both efficient cellular uptake and ionic assembly with the cluster anions. For these purposes silica nanoparticles (60 ± 6 nm) decorated by average 3500 amino-groups per each nanoparticle (evaluated by the fluorescamine-based procedure [34]) (Fig. S1, in Supporting Information (SI)) were synthesized through the well-known water-in-oil microemulsion procedure. The size of the nanoparticles was intentionally kept below 100 nm in order to ensure sufficient cellular uptake [17,18]. The TEM images of the synthesized silica nanoparticles (SNs) along with the simplified synthetic scheme are presented in Fig. 1.

Amino-decorated silica nanoparticles commonly demonstrate high aggregation in neutral aqueous media [36]. Indeed, the aggregation behavior of our SNs is significant in aqueous solutions at neutral pHs. The electrokinetic potential values collected in Table 1 indicate that the SNs are positively charged, although the charging does not prevent their aggregation. The high basicity of amino-groups is the well-known reason for their protonation in neutral conditions. Thus, the presence of ammonium in the equilibrium with amino groups explains the positive charging of the SNs. Interparticle interactions through amino-ammonium hydrogen bonding are the reason for aggregation of the SNs, as revealed by DLS data (Table 1).

Aggregation of nanoparticles is a well-known factor decreasing their surface activity, which can both prevent ionic assembly of SNs with the cluster units and restrict cell internalization of the assembled nanoparticles. It is worth noting in this connection that PEGylation of nanoparticles is efficient route to increase their colloid stability [37,38]. Triblock copolymers are documented as promising alternate to PEGs in hydrophilic coating of nanoparticles for their colloid stabilization [39–41]. Electrostatic attraction of the ammonium groups at the surface of the SNs with triblock copolymer molecules is worth assuming as driving force of their assembly at the SNs surface. The choice of the triblock copolymer L64 with the formula $(PEO)_{13}(PPO)_{30}(PEO)_{13}$ as the building block for coating has been determined by our previous results on interaction of L64 molecules with $[\{Mo_6I_8\}I_6]^{2-}$ cluster units as the reason for increased water solubility of the cluster, as well as for its the strong and stable luminescence in aqueous solutions [27]. The water solubility of $[\{Mo_6I_8\}(CH_3COO)_6]^{2-}$, stability and luminescence of the cluster in aqueous solutions is indifferent to the presence of L64 (Fig. S2a,c in SI). Thus, the effect of L64 on both uploading of the cluster into the SNs and aggregation of the assembled nanoparticles was exemplified by $[\{Mo_6I_8\}(CH_3COO)_6]^{2-}$.

The synthetic procedure is worth preceding by the evaluation of the interaction between the SNs and oppositely charged cluster units. Average particle size and electrokinetic potentials of the SNs in aqueous solutions of the cluster complexes, as measured by DLS, are presented in Table 1. The data (Tables 1 and S1) point to the charge neutralization and recharging of the SNs in the aqueous solutions of the cluster complexes.

Table 1
Mean size (d), electrokinetic potential (ζ) values, and polydispersity indices (PDI) for the SNs in water and aqueous solution of L64 (0.06 mM), for the SNs in the presence $[\{Mo_6I_8\}I_6]^{2-}$ and $[\{Mo_6I_8\}(CH_3COO)_6]^{2-}$ in aqueous solutions, and for the assembled C-SNs $[\{Mo_6I_8\}I_6]$-SNs and $[\{Mo_6I_8\}(CH_3COO)_6]$-SNs, where the assembly was facilitated by adding L64, as well as for $[\{Mo_6I_8\}(CH_3COO)_6]$-SNs* synthesized without L64.

	d[b], nm	PDI[b]	ζ[b], mV
SNs	1291 ± 232	0.657	+24 ± 0.7
SNs[a]	341 ± 1	0.222	+26 ± 0.5
$[\{Mo_6I_8\}(CH_3COO)_6]$-SNs	228 ± 6	0.201	+53 ± 1
$[\{Mo_6I_8\}(CH_3COO)_6]$-SNs*	784 ± 18	0.401	+48 ± 0.4
$[\{Mo_6I_8\}I_6]$-SNs	235 ± 5	0.145	+42.3 ± 7.6
$[\{Mo_6I_8\}(CH_3COO)_6]^{2-}$ + SNs	3225 ± 135	1.000	+13 ± 0.5
$[\{Mo_6I_8\}(CH_3COO)_6]^{2-*}$ + SNs	1658 ± 221	0.882	−16 ± 1
$[\{Mo_6I_8\}I_6]^{2-}$ + SNs	361 ± 3	0.168	−40 ± 0.6

[a] In aqueous solution of L64.
[b] d, ζ and PDI values were averaged from three independent experiments with the use of multiple scans (6–20) within each measurement.

The synthetic procedure for an assembly of the cluster units with the SNs was based on the mixing of the nanoparticulate and ionic components followed by centrifugation-mediated phase separation in order to remove excess of water soluble components from the separated colloid phase (for more details see Experimental). The efficiency of the cluster transfer (E%) from the solution to the nanoparticulate phase was evaluated from the UV–Vis spectral changes of aqueous solutions before and after their mixing with the nanoparticles followed by the phase separation through the centrifugation at various temperature conditions (Fig. S3 and Table S2 in SI). The presented E%-values (Table S2 in SI) were averaged from three independent experiments at the specific temperature conditions with the standard deviation about 1%. The data (Table S2 in SI) indicate significant dependence of the E%-values on temperature conditions of the centrifugation-induced phase separation. Thus, 25 °C is revealed as the optimal temperature of the centrifugation procedure to achieve highest E%-values (92.5% and 76% for $[\{Mo_6I_8\}I_6]^{2-}$ and $[\{Mo_6I_8\}(CH_3COO)_6]^{2-}$, correspondingly).

The transfer is evident visually, because white silica nanoparticles become colored after their ionic assembly with the cluster complexes. This is illustrated by photos at Fig. 2a, while the simultaneous de-coloration of the supernatant solutions was confirmed by the UV–Vis spectral measurements (Fig. S3 in SI). The separated nanoparticulate phase was re-dispersed in water or in the buffer solution. The assembled hybrid nanoparticles incorporate 0.0322 mmol of $[\{Mo_6I_8\}I_6]^{2-}$ and 0.0266 mmol of $[\{Mo_6I_8\}(CH_3COO)_6]^{2-}$ per 0.5 $g{\cdot}L^{-1}$ of the SNs. The weight of one nanoparticle was calculated by equation $m = 4/3{\cdot}\rho{\cdot}\pi{\cdot}r^3$, where density of the nanoparticles (ρ) is equal to pure silica (1.96 g/cm^3) and r is their average radius [42,43]. Assuming that m is $2.2{\cdot}10^{-16}$ g, we obtain

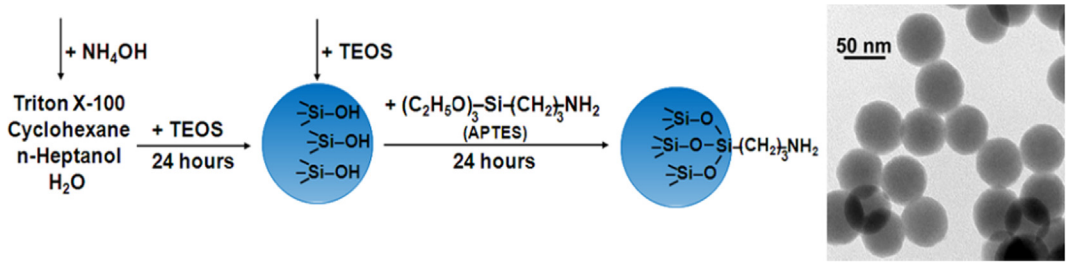

Fig. 1. Schematic representation of the synthesis and TEM image of the SNs.

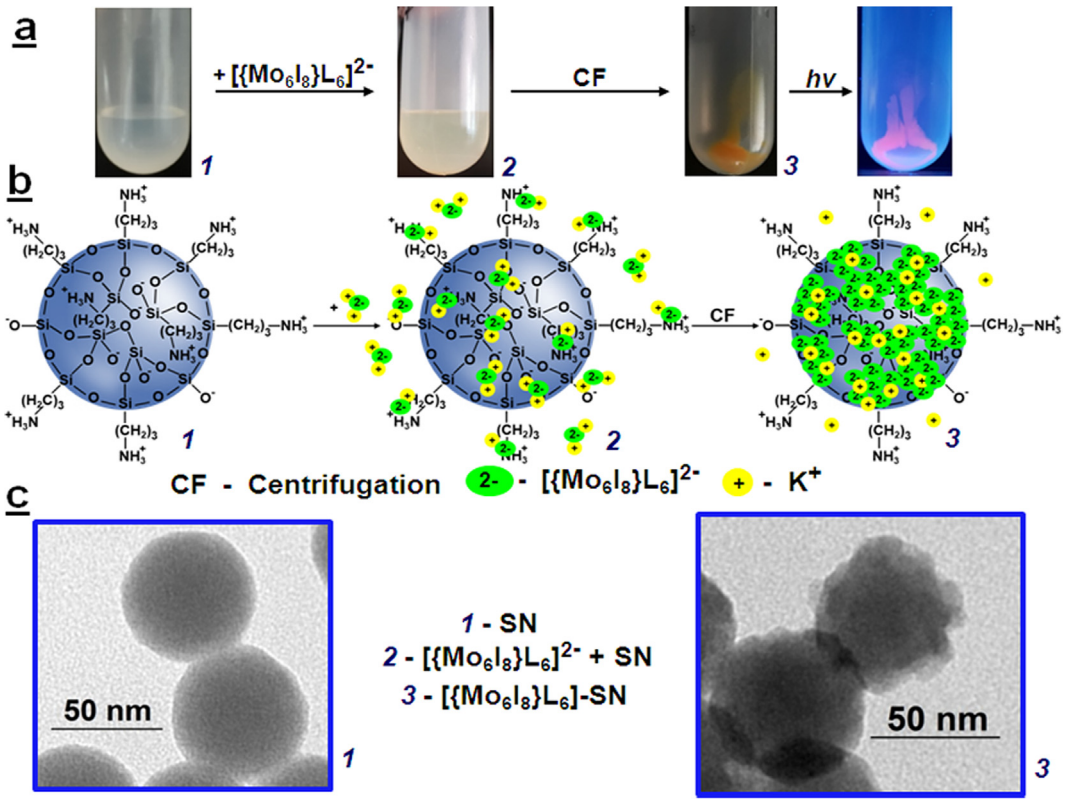

Fig. 2. (a) Photos of SNs in aqueous solution (1), SNs in the cluster solutions (2) and assembled SNs with clusters (3) before and after irradiation; (b) Schematic representation of self-assembly of the clusters complexes on silica surface; (c) TEM images of the SNs and $[\{Mo_6I_8\}(L)_6]$-SNs.

that each SN is decorated, in average, by 8700 $[\{Mo_6I_8\}I_6]^{2-}$ and 7100 $[\{Mo_6I_8\}(CH_3COO)_6]^{2-}$ cluster anions.

The assembled SNs will be further designated as $[\{Mo_6I_8\}I_6]$-SNs and $[\{Mo_6I_8\}(CH_3COO)_6]$-SNs where the charges are omitted for clarity, while the nanoparticles designated as $[\{Mo_6I_8\}(CH_3COO)_6]$-SNs* will refer to those synthesized without L64.

The assembled nanoparticles exhibit high positive charge (Table 1), while the charge neutralization of the SNs is observed in the aqueous solutions of the cluster at the same concentrations (Tables 1 and Fig. S1). The returning of the positive charge of SNs after the centrifugation step (Table 1) points to the centrifugation as a factor facilitating physical adsorption of the cluster complexes onto silica surface. Moreover, the centrifugation of the naked silica nanoparticles in aqueous solutions of $K_2[\{Mo_6I_8\}I_6]$ and $(nBu_4N)_2[\{Mo_6I_8\}(CH_3COO)_6]$ results in the detectable transfer of the cluster units from aqueous to silica phase, as manifested by the E%-values, 27% and 50% for $(nBu_4N)_2[\{Mo_6I_8\}(CH_3COO)_6]$ and $K_2[\{Mo_6I_8\}I_6]$ correspondingly. The naked silica nanoparticles are negatively charged, which restricts their interaction with the anionic cluster units but facilitates adsorption of potassium ions. Thus, these results point to the centrifugation as the reason for adsorption of both cluster salts onto the surface of the SNs and their naked analogues, but the efficiency of the cluster complexes transfer depends on the surface modification of the nanoparticles, being higher for the SNs decorated by amino groups. Nevertheless, both attraction of the cluster anions by ammonium groups and potassium ions by $Si\text{-}O^-$-groups are the driving forces for the efficient loading. The cartoon images in Fig. 2b illustrate both interactions.

The TEM-images of the assembled nanoparticles in Fig. 2c reveal the outgrowths at the silica surface which most probably derive from the attached cluster complexes. The lack of the outgrowths in the TEM images of the SNs separated from the L64-based aqueous solutions without the clusters confirms this assumption (Fig. S4 in SI). The recharging of the SNs in the solutions of the clusters indicate that the interaction between the negatively and positively charged groups at the silica surface with the cluster complexes tends to concentrate the latter at the silica/water interface. Thus, the reestablishment of the positive charge on the assembled SNs after the centrifugation step indicates switching of the interaction mode from the electrostatically driven cluster-silica interactions to the self-assembly of the clusters complexes at the silica/water interface (Fig. 2b).

The presence of L64 in the synthetic mixture causes insignificant effect on the E%-values for the uploading of $(nBu_4N)_2[\{Mo_6I_8\}(CH_3COO)_6]$ (Table S2 in SI). However, the DLS measurements reveal significant improvement of the aggregation behavior of the assembled nanoparticles in this case, which is evident from the lower polydispersity index (PDI) and mean particle size values, measured by DLS for $[\{Mo_6I_8\}(CH_3COO)_6]$-SNs where the ionic assembly was facilitated by L64 against L64-free $[\{Mo_6I_8\}(CH_3COO)_6]$-SNs* (Table 1).

The efficiency of the assembly procedure is confirmed by determination of Mo and Si contents by inductively coupled plasma optical emission spectrometry (ICP-OES) techniques. The data are listed in Table S3 in SI. The Mo:Si molar ratios calculated from the E% values (1:46 and 1:52 for $[\{Mo_6I_8\}I_6]$-SNs and $[\{Mo_6I_8\}(CH_3COO)_6]$-SNs) confirm the ratios calculated from the ICP-OES data (1:46 and 1:61 correspondingly).

3.2. Photophysical characteristics of $[\{Mo_6I_8\}(CH_3COO)_6]$-SNs and $[\{Mo_6I_8\}I_6]$-SNs and their stability in aqueous solutions.

Stability in time of the cluster-centered luminescence is one of the key requirements for their applicability in bioanalysis. Presentation of the photophysical characteristics of the assembled hybrid nanoparticles and discussion of their stability in time is worth

preceding by similar results for free cluster complexes in aqueous solutions. The luminescence of the both clusters suffers from the degradation in the MES-based buffer solutions (Fig. 3a and b). It is also worth noting that dissolution of $[\{Mo_6I_8\}(CH_3COO)_6]^{2-}$ in the buffer solution is accompanied by greater shifting of the emission band in the comparison with $[\{Mo_6I_8\}I_6]^{2-}$ under the same conditions (Fig. 3a and b).

The cluster-centered luminescence of $[\{Mo_6I_8\}(CH_3COO)_6]$-SNs is shifted to red (~10 nm) versus the luminescence of $[\{Mo_6I_8\}(CH_3COO)_6]^{2-}$ in the buffer solution (Fig. 3c), while the emission band of $[\{Mo_6I_8\}I_6]$-SNs is very similar to that of $[\{Mo_6I_8\}I_6]^{2-}$ in the aqueous solutions. The steady state and time resolved luminescence measurements were performed for the cluster complexes and C-SNs ($[\{Mo_6I_8\}I_6]$-SNs and $[\{Mo_6I_8\}(CH_3COO)_6]$-SNs) in the MES-buffered solutions, both within few minutes after the sample preparation and after long (within 10 days and 3 months) storage. The steady state spectra are shown in Fig. 3 and Fig. S2 in SI. The excited state lifetime values (τ) of the cluster complexes and C-SNs are collected in Table 2, the corresponding decay curves are shown in Fig. S5 in SI. The storage for 10 days of C-SNs is enough for detectable changes in both steady state luminescence spectra (Fig. 3) and τ-values (Table 2). The luminescence of the free cluster complexes in the solutions significantly decreases after the longer storage (Fig. S2 in SI), while only insignificant changes in the steady state spectra are observed for $[\{Mo_6I_8\}I_6]$-SNs and $[\{Mo_6I_8\}(CH_3COO)_6]$-SNs after their storage even for three months in the buffered solutions (Fig. S2 in SI). The τ-values of the clusters in molecular and nanoparticulate forms presented in Table 2 confirm the time-induced changes in cluster-centered luminescence for the both forms. Taking into account the well-known essential inertness of the apical ligands in hexamolybdenum clusters [44–47] the time-induced changes in both steady state and time resolved luminescence of the clusters in molecular and nanoparticulate forms can be explained by slow apical ligands (iodide or acetate) substitution. However, the difference between substitution processes in solutions and at the surface of the nanoparticles is worth noting. Quenching of the cluster-centered luminescence in solutions can be explained by both aquation and hydrolysis of the cluster complexes, while the substitution of the apical ligands by the plentiful amino and siloxy groups restricts aquation and suppresses hydrolysis of the clusters in C-SNs, which leads to the observed stability of the cluster-centered luminescence for $[\{Mo_6I_8\}I_6]$-SNs and $[\{Mo_6I_8\}(CH_3COO)_6]$-SNs. The cartoon image in Fig. 4 illustrates the anchoring of the cluster units at the silica surface *via* amino and siloxy groups through the apical ligand substitution.

Table 2
The excited state lifetime values (τ) of $[\{Mo_6I_8\}I_6]$-SNs, $[\{Mo_6I_8\}(CH_3COO)_6]$-SNs, $[\{Mo_6I_8\}I_6]^{2-}$ and $[\{Mo_6I_8\}(CH_3COO)_6]^{2-}$ in MES buffer solutions in the aerated conditions measured within few minutes after the sample preparation and after the storage for ten days and three months, $C_{cluster}$ = 0.035 mM, C_{SNs} = 0.5 g·L^{-1}, C_{MES} = 50 - mM (pH 7).

	τ, ms	τ (10 days), ms	τ (3 months), ms
$[\{Mo_6I_8\}I_6]$-SNs	0.03167 ± 0.00026	0.02215 ± 0.00017	0.02956 ± 0.00031
$[\{Mo_6I_8\}I_6]^{2-}$	0.03479 ± 0.00073	0.02533 ± 0.0004	–
$[\{Mo_6I_8\}(CH_3COO)_6]$-SNs	0.01534 ± 0.00024	0.02099 ± 0.00007	
$[\{Mo_6I_8\}(CH_3COO)_6]^{2-}$	0.02717 ± 0.00011	0.01324 ± 0.00051	
	0.02438 ± 0.00104	–	

Thus, both stability of the photophysical properties of $[\{Mo_6I_8\}(CH_3COO)_6]$-SNs, $[\{Mo_6I_8\}(CH_3COO)_6]$-SNs* and $[\{Mo_6I_8\}I_6]$-SNs nanoparticles and their specific morphology with the interfacial localization of the cluster units are worth regarding as promising basis for fluorescent cellular imaging and photodynamic therapy applications in the case of their high cell internalization and low cytotoxicity.

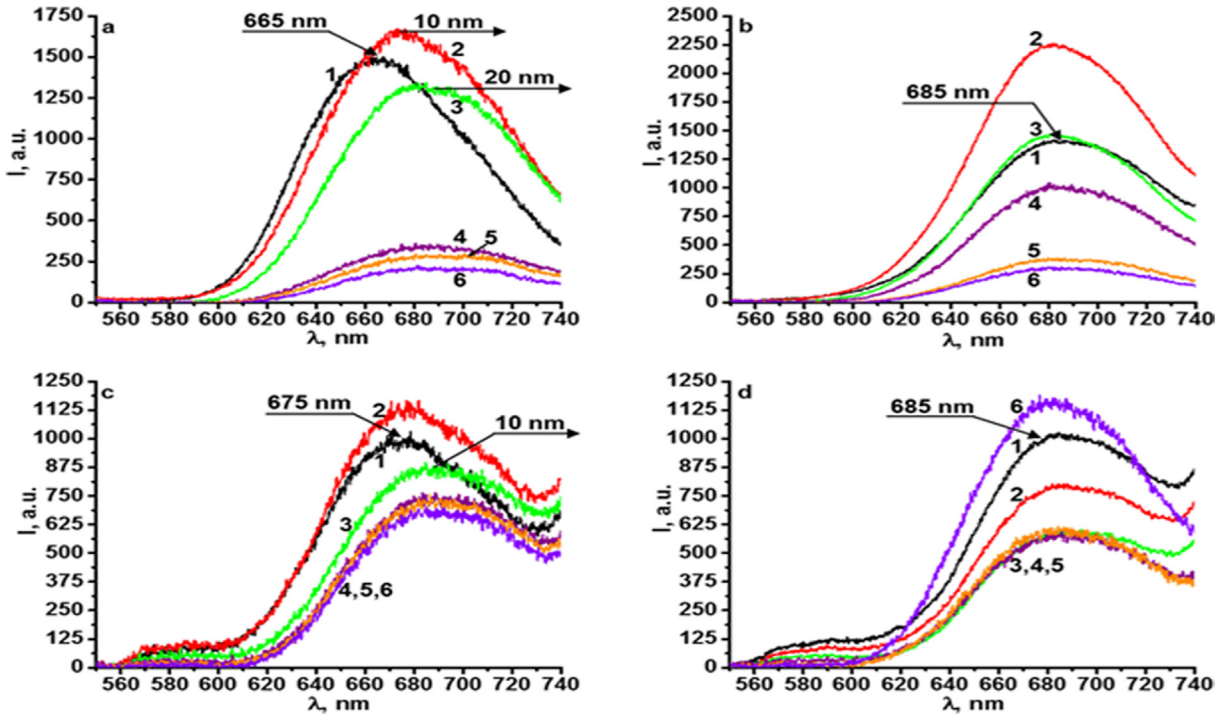

Fig. 3. Luminescence spectra of: $[\{Mo_6I_8\}(CH_3COO)_6]^{2-}$ (a) and $[\{Mo_6I_8\}I_6]^{2-}$ (b) in MES buffer solutions (a, b), $[\{Mo_6I_8\}(CH_3COO)_6]$-SNs (c) and $[\{Mo_6I_8\}I_6]$-SNs (d) in buffer solution at various time after the sample preparation: 5 min (1), 90 min (2), 1 day (3), 5 days (4), 8 days (5), 10 days (6). $C_{Cluster}$ = 0.035 mM, C_{SNs} = 0.5 g·L^{-1}, C_{MES} = 50 mM (pH 7), λ_{ex} = 380 nm.

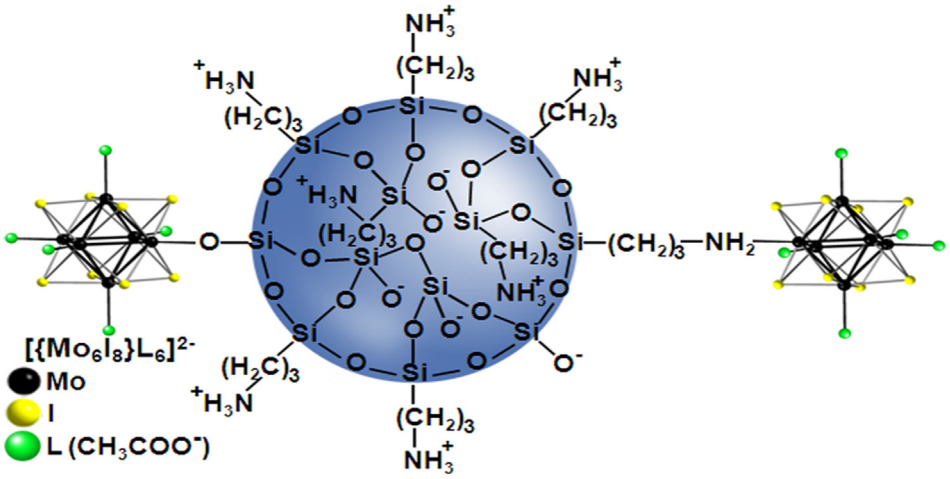

Fig. 4. Schematic representation of the anchoring of the cluster units at the silica surface *via* amino and siloxy groups.

3.3. Monitoring of the ROS generation by EPR measurements in aqueous solutions of [{Mo_6I_8}I_6]-SNs and [{Mo_6I_8}$(CH_3COO)_6$]-SNs

Generation of the highly reactive singlet oxygen $O_2(^1\Delta g)$ through energy transfer between excited triplet states of the cluster complexes and oxygen has attracted great attention in the recent decade due to its bactericidal [26,48] and antitumor activity [49,50]. Generation of ROS can be visualized by different techniques based on the use of specific luminophores, chromophores or magnetic probes able to change their functional properties in the presence of ROS [51]. The greater activity of $[\{Mo_6I_8\}(CH_3COO)_6]^{2-}$ versus $[\{Mo_6I_8\}I_6]^{2-}$ in the ROS-generation has been already documented by the use of the spectral assays for monitoring of $O_2(^1\Delta g)$. To the best of our knowledge, the cluster-mediated ROS-generation has been never monitored by the ESR technique facilitated by the spin traps, although the technique is highlighted as the most sensitive among others [30,31]. Moreover, the ESR technique enables to monitor generation of ROS under different regimes of the sample irradiation straight in the cell of the ESR spectrometer. The well-known spin trap DMPO (0.1 M) was applied for detection of the short-living radicals, since $O_2(^1\Delta g)$ itself is silent in X-band ESR spectroscopy, while its interaction with DMPO generates long-living spin adducts DMPO-OH [52], as manifested by peculiar ESR pattern.

The ESR measurements with the clusters in molecular and nanoparticulate forms were preceded by measuring the irradiation-induced changes in the ESR spectra of aqueous solution of DMPO in order to find optimal irradiation regime where the photolysis of water molecules would be insignificant [28]. The generation of spin-adducts in the aqueous solution of DMPO under irradiation at 365 nm by UV-lamp, and the lack of the paramagnetic species under the irradiation at 420 nm point to the latter irradiation conditions as optimal for the lack of water molecules photolysis.

The irradiation of aqueous solutions of DMPO in the presence of the clusters in both molecular and nanoparticulate forms gives rise to four resolved ESR signals. They can be simulated with the following parameters: g = 2.0055, a_N = 14.8 G, a_H = 14.8 G, ΔH = 0.7 G, which are characteristic for the DMPO-OH spin adduct [53]. Fig. 5 exemplifies the ESR spectrum for [{Mo_6I_8}$(CH_3COO)_6$]-SNs, the spectra generated with [{Mo_6I_8}$(CH_3COO)_6$]-SNs* and [{Mo_6I_8}I_6]-SNs (Fig. S6 in SI) being very similar to that in Fig. 5. The ESR signal appears at the beginning of irradiation and tends to increase in intensity within 10–15 min, which points to attainment of the steady state condition when rates of generation and decay of the spin-adducts become equal. When the irradiation is stopped, the signal gradually disappears, but is restored after repeated irradiation. Thus, irradiation within 15 min is enough for detectable

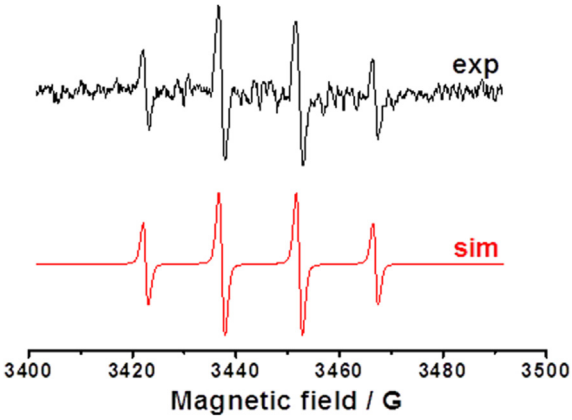

Fig. 5. Irradiation-generated ESR spectra in aqueous solution of DMPO (0.1 M) and [{Mo_6I_8}$(CH_3COO)_6$]-SNs (0.1 mM of the cluster units).

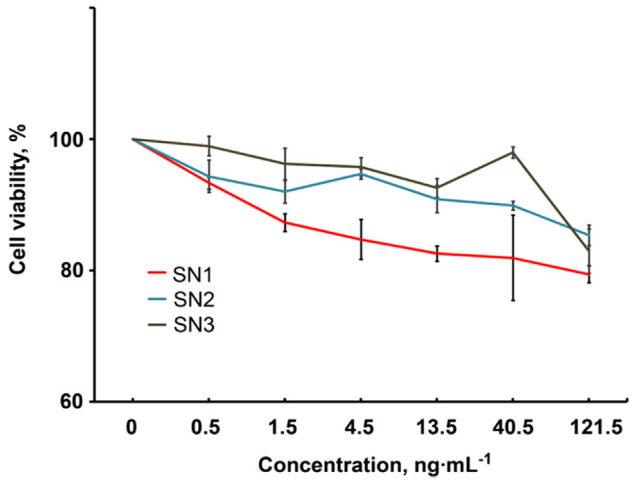

Fig. 6. Cell viability of MCF-7 incubated by [{Mo_6I_8}I_6]-SNs (SN1), [{Mo_6I_8}$(CH_3COO)_6$]-SNs* (SN2) and [{Mo_6I_8}$(CH_3COO)_6$]-SNs (SN3).

ROS generation. Similarity in the appearance of the ESR signal for the clusters in both molecular and nanoparticulate forms is also worth noting.

3.4. Cellular uptake and cytotoxicity of [{Mo_6I_8}$(CH_3COO)_6$]-SNs and [{Mo_6I_8}I_6]-SNs

The cell viability data measured for MCF-7 cell line are presented in Fig. 6. No significant toxicity is observed within the indicated concentration range, and the cell viability data reveal no difference between the nanoparticles.

Fluorescent measurements of MCF-7 cellular samples after incubation with the hybrid nanoparticles for 6 and 24 h indicate that 6 h of incubation is enough for efficient cellular uptake, which decreases after the longer incubation (Fig. 7). Cell internalization is detectably less for the normal cells, as is exemplified by HSF cell line after 6 h of the incubation (Fig. S7 in SI).

Thus, the assembled hybrid nanoparticles efficiently internalize the cells with rather low cytotoxic effect. This is the prerequisite for the applicability of the assembled nanoparticles as both cellular imaging and therapeutic agents. The latter function correlates with the ability of the clusters assembled to the SNs to generate ROS.

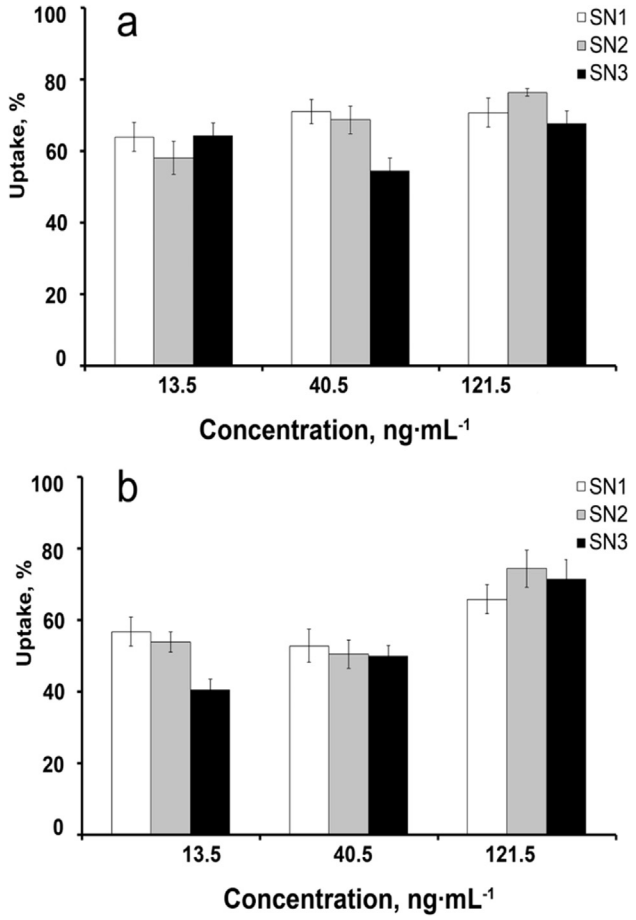

Fig. 7. Cell internalization of [{Mo_6I_8}I_6]-SNs (SN1), [{Mo_6I_8}$(CH_3COO)_6$]-SNs* (SN2) and [{Mo_6I_8}$(CH_3COO)_6$]-SNs (SN3) into MCF-7 after the incubation for 6 h (a) and 24 h (b).

3.4.1. Generation of ROS and photodynamic therapy effect

The cytotoxic effect from the generation of ROS was exemplified by the measurements of the cell viability data for MCF-7 and HSF cell lines by MTT assay. After incubation with nanoparticles the cells were irradiated at 420 nm for 15 min (for more details see Experimental).

The viability of the HSF cells incubated with nanoparticles and treated with 420 nm light was found to be around 65–80% for all three types of C-SNs (Fig. 8), i.e., the effect of the photodynamic treatment on the cell viability is rather low. By contrary, incubation with led to significant reduction in MCF-7 cells viability, up to 20 and 10% respectively (Fig. 8). The viability of MCF7 cells incubated with [{Mo_6I_8}I_6]-SNs was also reduced under the irradiation, although the reduction is less pronounced than for the cells incubated with [{Mo_6I_8}$(CH_3COO)_6$]-SNs and [{Mo_6I_8}$(CH_3COO)_6$]-SNs* (Fig. 8). The greater photodynamic effect of the SNs loaded by [{Mo_6I_8}$(CH_3COO)_6$]$^{2-}$ versus [{Mo_6I_8}I_6]-SNs on the cancer cells is in good agreement with the greater luminescence quantum yield and oxygen quenching constant of [{Mo_6I_8}$(CH_3COO)_6$]$^{2-}$ versus [{Mo_6I_8}$(I)_6$]$^{2-}$ [7,21]. Light treatment of the cells with nanoparticles led to the formation of ROS and a marked decrease in the viability of the cells of the breast cancer line. Thus, the generation of ROS is a main mechanism of the nanoparticles cytotoxicity, that causes DNA and RNA damage, oxidations of amino acids in proteins, increased lipid peroxidation and elevated expression of ROS responsive genes. Since the degree of internalization in the MCF-7 cells of all the investigated nanoparticles was very close, the different photodynamic effects are to be explained by different levels of ROS generation. What is important, is that lack of the toxic effect of the irradiation on human fibroblast cells incubated with the nanoparticles was observed (Fig. 8). This remarkable specificity of the cluster-generated photodynamic therapy allows targeted use of nanoparticles [{Mo_6I_8}$(CH_3COO)_6$]-SNs and

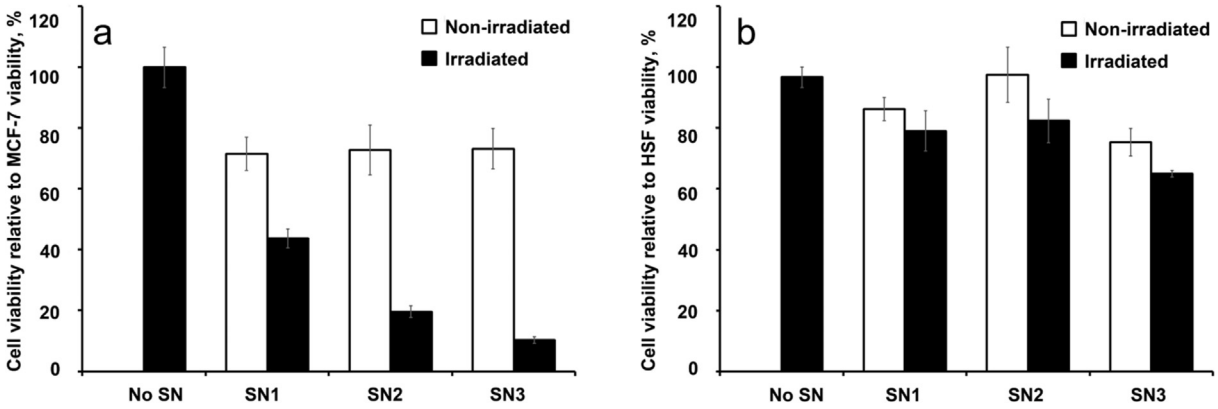

Fig. 8. The cell viability of irradiated (black) and non-irradiated (white) MCF-7 (a) and HSF (b) cell lines both non-treated by the SNs (No SN) and incubated with 121.5 ng·mL^{-1} of the C-SNs: [{Mo_6I_8}I_6]-SNs (SN1), [{Mo_6I_8}$(CH_3COO)_6$]-SNs* (SN2) and [{Mo_6I_8}$(CH_3COO)_6$]-SNs (SN3) after the irradiation at 420 nm.

[{Mo_6I_8}$(CH_3COO)_6$]-SNs* for therapy of oncological diseases. It is also worth noting that longer irradiation (for 30 min) and greater amount of the nanomaterial (about 0.1 mg·mL^{-1}) is required to produce significant killing of the cancer cells for the silica nanoparticles where {Mo_6I_8}-based cluster units are encapsulated into the silica matrix [50].

4. Conclusion

The present report introduces deposition of the luminescent hexamolybdenum cluster complexes onto amino-decorated silica nanoparticles as more facile and efficient loading technique versus the previously reported encapsulation of the cluster complexes into silica nanoparticles [7,8]. The deposition is initiated by electrostatic attraction of the cluster anions and their counter-ions to ammonium and siloxy groups at the silica surface. The centrifugation-induced separation of the nanoparticulate phase from the aqueous solution facilitates the deposition resulting in the positively charged nanoparticles loaded by ~8700 and ~7100 of K_2[{Mo_6I_8}I_6] and K_2[{Mo_6I_8}$(CH_3COO)_6$] cluster complexes per the nanoparticle. Both time-induced changes of the cluster-centered luminescence and the lack of the cluster complexes degradation point to an anchoring of the cluster units at the silica surface *via* amino and siloxy groups through the apical ligand substitution as the slow process which follows initial fast electrostatic binding. In this way we have achieved stable in time cluster-centered luminescence of the nanoparticles, arisen from the interfacial localization of the cluster units, which is a prerequisite for fluorescent cellular imaging and photodynamic therapy applications. The high cell internalization and low dark cytotoxicity of the loaded nanoparticles results from their positive charge and high stability of the cluster units. Localization of the cluster units at the silica/water interface exhibit some advantages in photodynamic effect on the cancer cells versus the nanoparticles where the {Mo_6I_8}-based cluster units are encapsulated into the silica matrix [50]. Moreover, the less irradiation-induced cytotoxicity is revealed for the non-cancerous cells. The specificity of the cluster-generated photodynamic therapy highlights [{Mo_6I_8}$(CH_3COO)_6$]-SNs and [{Mo_6I_8}$(CH_3COO)_6$]-SNs* as promising basis for photodynamic therapy of oncological diseases.

Acknowledgements

The authors gratefully acknowledge the Assigned Spectral-Analytical Center of FRC Kazan Scientific Center of RAS.

Appendix A. Supplementary data

Supplementary data to this article can be found online at https://doi.org/10.1016/j.jcis.2018.12.013.

References

[1] B. Fu, X. Huang, J. Deng, D. Gu, Q. Mei, M. Deng, S. Tang, M. Lü, Application of multifunctional nanomaterials in cancer vaccines (review), Oncol. Rep. 39 (2018) 893–900.
[2] M.-H. He, L. Chen, T. Zheng, Y. Tu, Q. He, H.-L. Fu, J.-C. Lin, W. Zhang, G. Shu, L. He, Z.-X. Yuan, Potential applications of nanotechnology in urological cancer, Front. Pharmacol. 9 (2018) 745.
[3] L. Feng, C. Wang, C. Li, S. Gai, F. He, R. Li, G. An, C. Zhong, Y. Dai, Z. Yang, P. Yang, Multifunctional theranostic nanoplatform based on Fe-mTa_2O_5@CuS-ZnPc/PCM for bimodal imaging and synergistically enhanced phototherapy, Inorg. Chem. 57 (2018) 4864–4876.
[4] J.G. Elistratova, K.A. Brylev, A.O. Solovieva, T.N. Pozmogova, A.R. Mustafina, L.V. Shestopalova, M.A. Shestopalov, V.V. Syakayev, A.A. Karasik, O.G. Sinyashin, Supporting effect of polyethylenimine on hexarhenium hydroxo cluster complex for cellular imaging applications, J. Photochem. Photobiol. A 340 (2017) 46–52.
[5] A.A. Krasilnikova, M.A. Shestopalov, K.A. Brylev, I.A. Kirilova, O.P. Khripko, K.E. Zubareva, Y.I. Khripko, V.T. Podorognaya, L.V. Shestopalova, V.E. Fedorov, Y.V. Mironov, Prospects of molybdenum and rhenium octahedral cluster complexes as X-ray contrast agents, J. Inorg. Biochem. 144 (2015) 13–17.
[6] A.O. Solovieva, K. Kirakci, A.A. Ivanov, P. Kubát, T.N. Pozmogova, S.M. Miroshnichenko, E.V. Vorontsova, A.V. Chechushkov, K.E. Trifonova, M.S. Fufaeva, E.I. Kretov, Yu.V. Mironov, A.F. Poveshchenko, K. Lang, M.A. Shestopalov, Singlet oxygen production and biological activity of hexanuclear chalcocyanide rhenium cluster complexes [{R_{e6Q8}}$(CN)_6^{4-}$ (Q = S, Se, Te), Inorg. Chem. 56 (2017) 13491–13499.
[7] N. Brandhonneur, T. Hatahet, M. Amela-Cortes, Y. Molard, S. Cordier, G. Dollo, Molybdenum cluster loaded PLGA nanoparticles: an innovative theranostic approach for the treatment of ovarian cancer, Eur. J. Pharm. Biopharm. 125 (2018) 95–105.
[8] K. Kirakci, V. Sícha, J. Holub, P. Kubát, K. Lang, Luminescent hydrogel particles prepared by self-assembly of β-cyclodextrin polymer and octahedral molybdenum cluster complexes, Inorg. Chem. 53 (2014) 13012–13018.
[9] M.H. Raza, S. Siraj, A. Arshad, U. Waheed, F. Aldakheel, S. Alduraywish, M. Arshad, ROS-modulated therapeutic approaches in cancer treatment, J. Cancer Res. Clin. Oncol. 143 (2017) 1789–1809.
[10] B.I. Tamba, A. Dondas, M. Leon, A.N. Neagu, G. Dodi, C. Stefanescu, A. Tijani, Silica nanoparticles: preparation, characterization and in vitro/in vivo biodistribution studies, Eur. J. Pharm. Sci. 71 (2015) 46–55.
[11] M.C. Gomes, Â. Cunha, T. Trindade, J.P.C. Tomé, The role of surface functionalization of silica nanoparticles for bioimaging, J. Innov. Opt. Health Sci. 9 (2016) 1630005-1–1630005-16.
[12] J. Wang, Z.H. Shah, S. Zhang, R. Lu, Silica-based nanocomposites via reverse microemulsions: classifications, preparations and applications, Nanoscale 6 (2014) 4418–4437.
[13] A.R. Mukhametshina, S.V. Fedorenko, A.M. Petrov, G.F. Zakyrjanova, K.A. Petrov, L.F. Nurullin, I.R. Nizameev, A.R. Mustafina, O.G. Sinyashin, Targeted nanoparticles for selective marking of neuromuscular junctions and *ex vivo* monitoring of endogenous acetylcholine hydrolysis, ACS Appl. Mater. Interfaces 10 (2018) 14948–14955.
[14] C.M. Beddoes, C.P. Case, W.H. Briscoe, Understanding nanoparticle cellular entry: a physicochemical perspective, Adv. Colloid Interface Sci. 218 (2015) 48–68.
[15] S. Salatin, S.M. Dizaj, A.Y. Khosroushahi, Effect of the surface modification, size, and shape on cellular uptake of nanoparticles, Cell Biol. Int. 39 (2015) 881–890.
[16] K. Saha, S.T. Kim, B. Yan, O.R. Miranda, F.S. Alfonso, D. Shlosman, V.M. Rotello, Surface functionality of nanoparticles determines cellular uptake mechanisms in mammalian cells, Small 9 (2013) 300–305.
[17] A. Nel, T. Xia, L. Madler, N. Li, Toxic potential of materials at the nanolevel, Science 311 (2006) 622–627.
[18] H.M. Kipen, D.L. Laskin, Smaller is not always better: nanotechnology yields nanotoxicology, Am. J. Physiol.-Lung Cell. Mol. Physiol. 289 (2005) L696–L697.
[19] C. Graf, Qi. Gao, I. Schütz, C.N. Noufele, W. Ruan, U. Posselt, E. Korotianskiy, D. Nordmeyer, F. Rancan, S. Hadam, A. Vogt, J. Lademann, V. Haucke, E. Rühl, Surface functionalization of silica nanoparticles supports colloidal stability in physiological media and facilitates internalization in cells, Langmuir 28 (2012) 7598–7613.
[20] A. Lesniak, F. Fenaroli, M.P. Monopoli, C. Åberg, K.A. Dawson, A. Salvati, Effects of the presence or absence of a protein corona on silica nanoparticle uptake and impact on cells, ACS Nano 6 (2012) 5845–5857.
[21] K. Kirakci, P. Kubát, M. Dusěk, K. Fejfarová, V. S ícha, J. Mosinger, K. Lang, A highly luminescent hexanuclear molybdenum cluster – a promising candidate toward photoactive materials, Eur. J. Inorg. Chem. (2012) 3107–3111.
[22] F. Cabello-Hurtado, M.D. Lozano-Baena, C. Neaime, A. Burel, S. Jeanne, P. Pellen-Mussi, S. Cordier, F. Grasset, Studies on plant cell toxicity of luminescent silica nanoparticles ($Cs_2[Mo_6Br_{14}]$@SiO_2) and its constitutive components, J. Nanopart. Res. 18 (2016) 69.
[23] F. Grasset, F. Dorson, Y. Molard, S. Cordier, V. Demange, C. Perrin, V. Marchi-Artznera, H. Haneda, One-pot synthesis and characterizations of bi-functional phosphor–magnetic @SiO_2 nanoparticles: controlled and structured association of Mo6 cluster units and c-Fe_2O_3 nanocrystals, Chem. Commun. (2008) 4729–4731.
[24] F. Grasset, F. Dorson, S. Cordier, Y. Molard, C. Perrin, A.-M. Marie, T. Sasaki, H. Haneda, Y. Bando, M. Mortier, Water-in-oil microemulsion preparation and characterization of $Cs_2[M_{o6}X_{14}]$@SiO_2 phosphor nanoparticles based on transition metal clusters (X = Cl, Br, and I), Adv. Mater. 20 (2008) 143–148.
[25] M. Amela-Cortes, Y. Molard, S. Paofai, A. Desert, J.-L. Duvail, N.G. Naumov, S. Cordier, Versatility of the ionic assembling method to design highly luminescent PMMA nanocomposites containing $[M_6Q_{i8}L_{a6}]^{n-}$ octahedral nano-building blocks, Dalton Trans. 45 (2016) 237–245.
[26] A. Beltrán, M. Mikhailov, M.N. Sokolov, V. Pérez-Laguna, A. Rezusta, M. Revillod, F. Galindo, A photobleaching resistant polymer supported hexanuclear molybdenum iodide cluster for photocatalytic oxygenations and photodynamic inactivation of Staphylococcus aureus, J. Mater. Chem. B 4 (2016) 5975–5979.
[27] J. Elistratova, M. Mikhailov, V. Burilov, V. Babaev, I. Rizvanov, A. Mustafina, P. Abramov, M. Sokolov, A. Konovalov, V. Fedin, Supramolecular assemblies of triblock copolymers with hexanuclear molybdenum clusters for sensing antibiotics in aqueous solutions *via* energy transfer, RSC Adv. 4 (2014) 27922–27930.

[28] A. Ancona, B. Dumontel, N. Garino, B. Demarco, D. Chatzitheodoridou, W. Fazzini, H. Engelke, V. Cauda, Lipid-coated zinc oxide nanoparticles as innovative ROS-generators for photodynamic therapy in cancer cells, Nanomaterials 8 (2018) 143.
[29] D.B. Tada, M.S. Baptista, Photosensitizing nanoparticles and the modulation of ROS generation, Front. Chem. 3 (2015) 33.
[30] K. Abbas, N. Babic, F. Reyrot, Use of spin traps to detect superoxide production in living cells by electron paramagnetic resonance (EPR) spectroscopy, Methods 109 (2016) 31–43.
[31] M. Carini, G. Aldini, M. Orioli, R.M. Facino, Electron paramagnetic resonance (EPR) spectroscopy: A versatile and powerful tool in pharmaceutical and biomedical analysis, Curr. Pharmac. Anal. 2 (2006) 141–159.
[32] E. Finkelstein, G.M. Rosen, E.J. Rauckman, Spin trapping of superoxide and hydroxyl radical: practical aspects, Arch. Biochem. Biophys. 200 (1980) 1–16.
[33] M.A. Mikhailov, K.A. Brylev, P.A. Abramov, E. Sakuda, S. Akagi, A. Ito, N. Kitamura, M.N. Sokolov, Synthetic tuning of redox, spectroscopic, and photophysical properties of $\{Mo_6I_8\}^{4+}$ core cluster complexes by terminal carboxylate ligands, Inorg. Chem. 55 (2016) 8437–8445.
[34] Y. Chen, Y. Zhang, Fluorescent quantification of amino groups on silica nanoparticle surfaces, Anal. Bioanal. Chem. 399 (2011) 2503–2509.
[35] A. Takashima, Establishment of fibroblast cultures, Curr. Protoc. Cell Biol. 2 (2001) 21.
[36] S.V. Fedorenko, A.R. Mustafina, A.R. Mukhametshina, M.E. Jilkin, T.A. Mukhametzyanov, A.O. Solovieva, T.N. Pozmogova, L.V. Shestopalova, M.A. Shestopalov, K.V. Kholin, Y.N. Osin, O.G. Sinyashin, Cellular imaging by green luminescence of Tb(III)-doped aminomodified silica nanoparticles, Mater. Sci. Eng. C 76 (2017) 551–558.
[37] M. Xie, H. Shi, Z. Li, H. Shen, K. Ma, B. Li, S. Shen, Y. Jin, A multifunctional mesoporous silica nanocomposite for targeted delivery, controlled release of doxorubicin and bioimaging, Colloids Surf. B 110 (2013) 138–147.
[38] S. Liu, Y. Han, R. Qiao, J. Zeng, Q. Jia, Y. Wang, M. Gao, Investigations on the interactions between plasma proteins and magnetic iron oxide nanoparticles with different surface modifications, J. Phys. Chem. C 114 (2010) 21270–21276.
[39] E. Rampazzo, S. Bonacchi, D. Genovese, R. Juris, M. Montalti, V. Paterlini, N. Zaccheroni, C. Dumas-Verdes, G. Clavier, R. Meallet-Renault, L. Prodi, Pluronic-silica (PluS) nanoparticles doped with multiple dyes featuring complete energy transfer, J. Phys. Chem. C 118 (2014) 9261–9267.
[40] J. Elistratova, B. Akhmadeev, A. Gubaidullin, V. Korenev, M. Sokolov, I. Nizameev, A. Stepanov, I. Ismaev, M. Kadirov, A. Voloshina, A. Mustafina, Nanoscale hydrophilic colloids with high relaxivity and low cytotoxicity based on Gd(III) complexes with Keplerate polyanions, New J. Chem. 41 (2017) 5271–5275.
[41] J. Elistratova, B. Akhmadeev, A. Gubaidullin, M.A. Shestopalov, A. Solovieva, K. Brylev, K. Kholin, I. Nizameev, I. Ismaev, M. Kadirov, A. Mustafina, Structure optimization for enhanced luminescent and paramagnetic properties of hydrophilic nanomaterial based on heterometallic Gd-Re complexes, Mater. Des. 146 (2018) 49–56.
[42] Z. Ye, M. Tan, G. Wang, J. Yuan, Preparation, characterization, and time-resolved fluorometric application of silica-coated terbium(III) fluorescent nanoparticles, Anal. Chem. 76 (2004) 513–518.
[43] S. Santra, P. Zhang, K. Wang, R. Tapec, W. Tan, Conjugation of biomolecules with luminophore-doped silica nanoparticles for photostable biomarkers, Anal. Chem. 73 (2001) 4988–4993.
[44] K. Kirakci, S. Cordier, C. Perrin, Synthesis and characterization of $Cs_2Mo_6X_{14}$ (X=Br or I) hexamolybdenum cluster halides: Efficient Mo_6 cluster precursors for solution chemistry syntheses, Z. Anorg. Allg. Chem. 631 (2005) 411–416.
[45] G.M. Ehrlich, H. Deng, L. Hill, M.L. Steigerwald, P.J. Squattrito, F.J. DiSalvo, Synthesis and characterization of cis-[Mo6Cl8(Cl4)(P(C2H5)3)2].cntdot.2THF, Inorg. Chem. 34 (1995) 2480–2482.
[46] C.B. Gorman, W.Y. Su, H. Jiang, C.M. Watson, P. Boyle, Hybrid organic–inorganic, hexa-arm dendrimers based on an Mo_6Cl_8 core, Chem. Commun. (1999) 877–878.
[47] N. Prokopuk, S. Weinert, D.P. Siska, C.L. Stern, D.F. Shriver, Hydrogen-bonded hexamolybdenum clusters: Formation of inorganic–organic networks, Angew. Chem. Int. Ed. 39 (2000) 3312–3315.
[48] M.R. Hamblin, T. Hasan, Photodynamic therapy: a new antimicrobial approach to infectious disease?, Photochem Photobiol. Sci. 3 (2004) 436–450.
[49] E. Dolmans, D. Fukumura, R.K. Jain, Photodynamic therapy for cancer, Nature Rev. Cancer 3 (2003) 380–387.
[50] A.O. Solovieva, Y.A. Vorotnikov, K.E. Trifonova, O.A. Efremova, A.A. Krasilnikova, K.A. Brylev, E.V. Vorontsova, P.A. Avrorov, L.V. Shestopalova, A. F. Poveshchenko, Y.V. Mironov, M.A. Shestopalov, Cellular internalisation, bioimaging and dark and photodynamic cytotoxicity of silica nanoparticles doped by $\{Mo_6I_8\}^{4+}$ metal clusters, J. Mater. Chem. B 4 (2016) 4839–4846.
[51] W. Tao, Z. He, ROS-responsive drug delivery systems for biomedical applications, Asian J. Pharm. Sci. 13 (2018) 101–112.
[52] C. Nishizawa, K. Takeshita, J.I. Ueda, M. Mizuno, K.T. Suzuki, T. Ozawa, Hydroxyl radical generation caused by the reaction of singlet oxygen with a spin trap, DMPO, increases significantly in the presence of biological reductants, Free Radical Res. 38 (2004) 385–392.
[53] W.R. Hedrick, M.D. Webb, J.D. Zimbrick, Spin trapping of reactive uracilyl radicals produced by ionizing radiation in aqueous solutions, Int. J. Radiat. Bio. Rel. Stud. Phys., Chem. Med. 41 (1982) 435–442.